Sensitivity of model estimates of CME propagation and arrival time to inner boundary conditions

Lauren A. James[1], Christopher J. Scott[1], Luke A. Barnard[1], Mathew J. Owens[1], Matthew S. Lang[1], and Shannon R. Jones[1].

[1]Department of Meteorology, University of Reading, Reading, UK

Key Points:

- Multiple fronts detected by STEREO's Heliospheric Imager can be used to describe the longitudinal distortion of a CME.
- Close-Sun distortion can be simulated in a reduced physics model using back mapping techniques.
- Relating ensemble time-elongation profile error and arrival time error can be used to estimate CME arrival to within 3 hours.

Corresponding author: Lauren A. James, l.a.james@pgr.reading.ac.uk

Abstract

Accurately forecasting the arrival of coronal mass ejections (CMEs) at Earth is important to enabling mitigation of the associated space weather risks to society. This is only possible with accurate modelling of the event. To do so, we must understand the propagation of a CME through the heliosphere and quantify the performance of models through comparison with spacecraft observations. For the December 12th 2008 Earth-directed CME event, we compute ensembles using the HUXt solar wind model to analyse CME distortion with a structured solar wind and explore hindcast arrival time error (ATE). By highlighting the impact CME shape has on Root-Mean-Square-Error (RMSE) values, we show that time-elongation profiles of fronts captured by the Heliospheric Imager (HI) instruments onboard NASA's STEREO mission match those of the modelled CME nose and flank and can therefore be used to infer details of the longitudinal extent of the CME. We then show that accounting for CME distortion is important to enable accurate estimates of the CME arrival at Earth. This can be achieved by either using observations of multiple features in HI data to infer CME evolution or mapping the solar wind back to a lower inner boundary to allow CMEs to be distorted close to the Sun. For the event studied we show that these approaches resulted in reduced RMSEs of 0.726and 0.638 with an ATE of one hour and three hours respectively.

Plain Language Summary

Coronal Mass Ejections (CMEs) are giant plasma "bubbles" that erupt from the Sun into space. Upon engulfing Earth, they interact with the near-Earth space environment and result in disruptions to modern electrical infrastructure. Therefore, accurately forecasting CME arrival time at Earth is vital in order to mitigate the risk of space weather. Here, for the December 12th 2008 Earth-directed event, we use a simple-physics solar wind model (HUXt) to explore the distortion that occurs to a CME throughout the journey from the Sun to Earth. Features of the leading edge are tracked from the viewpoint of two spacecraft (STEREO) that are positioned away from the Sun-Earth line and compared to position profiles of bright-light regions pictured by the mission's Heliospheric Imager camera. By running the HUXt model many times, we explore the relationship between the error of the tracked features and the arrival time error of the hindcast. We find that using multiple features to quantify model performance can improve the arrival time prediction, compared to tracking a single feature. Alternatively, we can account for changes to the CME geometry that occur close to the Sun by ejecting a CME into the model earlier.

1 Introduction

Coronal Mass Ejections (CME) are the major driver of severe space weather impacts (Cane & Richardson, 2000; Gosling, 1993). A CME is a cloud of magnetised plasma moving rapidly away from the Sun, at speeds varying from 300 $\mathrm{kms^{-1}}$ to 2500 $\mathrm{kms^{-1}}$ and containing $10^{12} - 10^{13}$ kg of material (Kahler, 1987; Riley & Gosling, 1997). On arrival at Earth, a CME can interact with Earth's magnetosphere, causing short-term changes to the planet's magnetic field, especially if the CME has a southward interplanetary magnetic field component (Dungey, 1961; Chao & Chen, 2001; Arnoldy, 1971). Due to modern civilization's increasing reliance on electrical technologies, society is more vulnerable to the impacts of "space weather". A CME can cause disruption to satellite communications, ground-based power grids and the air travel industry (to name but a few of the detrimental impacts)(Cannon, 2013). This highlights the importance of forecast accuracy for Earth-directed CMEs (Oughton et al., 2019; Hapgood & Thomson, 2018; Möstl et al., 2011; Davies et al., 2012; Barnard et al., 2017).

Currently, operational space weather forecasts typically rely on three-dimensional magnetohydrodynamic (3D MHD) models of the solar wind, with CME initial conditions being estimated by analysis of coronagraph data. Such models, like ENLIL (Odstrcil, 2003), are used by NOAA's Space Weather Prediction Center (SWPC) and the UK Met Office's Space Weather Operation Centre (MOSWOC) to produce deterministic and ensemble forecasts of CME arrival time at Earth (Mays et al., 2015; Pizzo et al., 2011). Due to the computing resources needed by full-physics models to run once, the number of ensemble runs are limited by feasibility (Lee et al., 2013; Cash et al., 2015), with the MOSWOC computing 24 runs in their forecast (Henley & Pope, 2017). Analysis of these forecasts reveal a CME mean arrival time error of approximately 13 hours (Riley et al., 2018; Mays et al., 2015; Vršnak et al., 2014; Iwai et al., 2021). An alternative approach used in recent research (e.g. Barnard et al., 2020; Chi et al., 2021) is to use a computationally efficient reduced-physics solar wind model (HUXt, Owens, Lang, Barnard, et al., 2020) to explore parameter space in ensembles with many hundreds to thousands of members. Such ensemble modelling methods can provide both robust uncertainty estimates and probabilistic forecasts (Barnard et al., 2020; Owens & Riley, 2017). It is anticipated that the results from these larger ensembles can ultimately be used to inform targeted ensemble runs using full 3D MHD solar wind models. We here present an analysis of the sensitivity of the HUXt model results to inner boundary conditions. In particular, we determine the accuracy with which HUXt can reproduce multiple CME fronts seen in spacecraft data, aiding our interpretation of such complex observations.

NASA's Solar TErrestrial RElations Observatory (STEREO) mission (Kaiser et al., 2008), launched in late 2006, was designed to further understand the initiation, structure, and the propagation of CMEs, especially for Earth directed events. Consisting of two spacecraft in heliocentric orbits, STEREO-A (STA) travels ahead of Earth while STEREO-B (STB) lags behind in such a way that they separate from Earth by approximately 22° of ecliptic longitude annually. Both STEREO spacecraft have the same instrument packages that take images of the Sun and solar wind, and in-situ measurements of solar wind plasma and magnetic fields. The remote sensing instrument package SECCHI (Sun–Earth Connection Coronal and Heliospheric Investigation) can provide information about the three-dimensional structural evolution of a CME. It includes white-light heliosperic imagers (HIs), white-light coronagraphs (COR) and an extreme ultraviolet imager (EUVI). Together, they observe space from the lower solar atmosphere to beyond 1AU. COR1 and COR2 cover 1.4 – 4 solar radii ($R_\odot$) and 2 $R_\odot$ – 15 $R_\odot$, respectively, while HI has a field of view from 15 $R_\odot$ to beyond Earth orbit at 215 $R_\odot$ (R. A. Howard et al., 2008). The heliospheric imager is composed of two cameras; HI-1 and HI-2, each with different fields of views that allow a CME to be tracked up to 88.7° elongation from the Sun (R. A. Howard et al., 2008; Eyles et al., 2009; Davis et al., 2009). This mission was the first to observe CME events from multiple viewpoints outside the Sun-Earth line.

The heliospheric imagers rely on Thomson scattering - the process of sunlight being scattered off free electrons (Billings, 1966; T. A. Howard & Deforest, 2012; Deforest et al., 2013; T. A. Howard et al., 2013) to generate their images. Each pixel contains an integration of the light scattered by plasma along that line of sight. As with conventional photography, an HI image is a two dimensional representation of three dimensional structure.

The first major Earth-directed CME was observed by STEREO on the December 12th 2008, and has since been the subject of a number of studies (Davis et al., 2009; Byrne et al., 2010; Lugaz et al., 2010; Liu et al., 2010; Deforest et al., 2011, 2012; Manchester et al., 2017; Zhang et al., 2019; T. A. Howard & Deforest, 2012). At this time, STA and STB were positioned approximately 42° and -44° from Earth respectively. For STB, this is a similar viewing geometry to the proposed ESA *Vigil* mission, formerly known as the *Lagrange* mission (Vourlidas, 2015; Thomas et al., 2018; Akioka et al., 2005), therefore, this event represents a useful study of CME observations from such a experiment. One previous study of this event (Davis et al., 2009) assumed the density enhancements seen in HI were discrete substructures within the CME and disturbed solar wind. By using the forecast front arrival times at L1, the behaviour of the magnetic and plasma measurements were shown to correlate to the properties of the leading edge, magnetic flux rope, and the core of the CME. Later, by assuming both STEREO spacecraft observed the same feature, a geometric triangulation technique out to 1AU with prescribed and fixed spherical (Lugaz et al., 2010) and non-spherical fronts (Liu et al., 2010) showed that the direction and distance of the CME could be tracked though the HI field of view to match the L1 in-situ observations. Mapping two-dimensional views seen in HI images to the complex, three-dimensional structures of CMEs is not straight forward. Barnard et al. (2017) demonstrated that assuming a CME retained a simple geometric shape as it propagated through the heliosphere was not consistent with the known uncertainties of the observations. More recently, Scott et al. (2019) suggested that a single three-dimensional leading edge could produce multiple regions (i.e. a nose and a flank) of enhanced Thomson scatter leading to multiple structures within a two dimensional HI image. For the December 12th 2008 event it was demonstrated that multiple features seen in HI images evolved in a way that was consistent with a Kinematically Evolving Flux Rope (Owens et al., 2006) expanding into a structured solar wind.

Here, we use the HUXt model, described below, to make multiple simulations of the December 12th 2008 CME using varying initial to produce elongation profiles and hindcasts. Through comparison with the multiple CME fronts observed by HI, we determine which experiment best reproduces the observations and whether good model performance leads to an improved estimate of the CME arrival time at Earth. We test to see how the inclusion of data assimilated solar wind at the inner boundary, the distance of the inner boundary and the assumed uncertainty in the initial parameters impact model output. These will be discussed in more detail in the following section.

2 Techniques

2.1 Solar Wind Data Assimilation

Near-Sun solar wind conditions which serve as the inner boundary conditions to heliospheric models are typically provided by coronal models constrained by the observed photospheric magnetic field (Linker et al., 1999; Arge et al., 2004; Holst et al., 2014, e.g. MAS, WAS, AWSoME). Here, we start with output from the MAS (Magnetohydrodynamic Algorithm outside a Sphere) model (Linker et al., 1999), but additionally assimilate the available in situ solar wind observations to provide a more accurate reconstruction of the ambient solar wind conditions.

The Burger Radial Variational Data Assimilation (BRaVDA) solar wind scheme (Lang & Owens, 2019; Lang et al., 2020) calculates an optimal inner boundary condition for a steady state simulation of the equatorial solar wind, through the assimilation of in-situ solar wind observations. A perturbation of the MAS model solution is defined as the prior state at the scheme's inner boundary and allowed to propagate out into the simulated heliosphere using the HUX model. Error between model and observation is computed with measurements from 1 AU spacecraft. By seeking the minimum cost function (sum of prior and observation squared errors, weighted by their relative uncertainties) in the scheme, an optimum inner boundary array is defined as the posterior state. The output array from BRaVDA can then be used to define a solar wind structure at 30 $R_\odot$ in a heliospheric models, such as HUXt.

In this study, NASA's Advanced Composition Explorer (ACE) is used to provide solar wind speed observations. Whilst multi-spacecraft observations are generally desirable to improve accuracy, STEREO A and B observations were not used here due to differences in solar wind structure that are likely the result of spacecraft heliographic latitude. A fast-stream was measured by STA but not in STB, suggesting large differences in solar wind structure over relatively small latitudinal ranges about the helio equator, an issue common during solar minimum (Owens, Lang, Riley, et al., 2020). Instead, in-situ data from ACE between 360° and 90° Carrington longitude (i.e., a full Carrington rotation excluding the time at which the CME interacted with the spacecraft) was used in the assimilation. Figure 1 shows time-series of solar wind speed at L1 produced by HUXt initialised with the non-data assimilated MAS solar wind conditions and the data assimilated solar wind conditions (BRaVDA), compared to real observations from the ACE spacecraft. Both model outputs produce peaks at the same periods seen in the observation, however, BRaVDA is shown to be better at not overestimating the speed or creating extra peaks. This is most noticeable on December 3rd 2008.

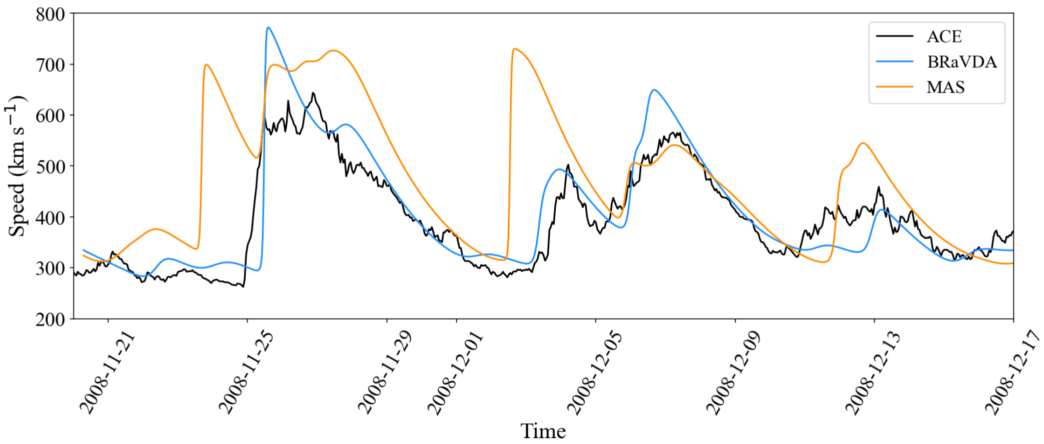

Figure 1. Time series of solar wind speed at L1 for real ACE data (black) and HUXt model output initialised at 30 $R_\odot$ with a non-data assimilated solar wind scheme (MAS; orange) and a data assimilated solar wind scheme (BRaVDA; blue). Dates ticks correspond to 00:00 UTC.

2.2 HUXt

The Heliospheric Upwind eXtrapolation model with time-dependency (HUXt; Owens, Lang, Barnard, et al., 2020) is a reduced physics numerical model used to simulate heliospheric conditions and CME propagation. To do this, the complex magnetic equations that are found in full-physics 3D models, like Enlil (Odstrcil, 2003), are simplified greatly, to the assumption that the plasma is a purely radial and behaves as an incompressible and inviscid hydrodynamic flow. In the steady-state approximation, this approach was shown to match 3D MHD output (Riley & Lionello, 2011) and has recently been adapted to allow for time-dependent solar wind structure (Owens, Lockwood, & Barnard, 2020). Even with the high level of physical approximation, HUXt can replicate the outwards movement of plasma to beyond 1AU within 5% accuracy of the full-physics models (Owens, Lockwood, & Barnard, 2020). Due to these simplifications, the time for a single run of HUXt takes a fraction of a second on your average desktop computer, significantly reduced compared with the full-physics models. The computational efficiency of this model enables the computation of many-member ensembles, as has been done by Barnard et al. (2020).

Within HUXt, CMEs are introduced as a velocity pulse at the inner boundary. The properties of this pulse are determined with information about the source latitude and longitude, width, speed, and thickness derived from cone-model fits to coronagraph images (Millward et al., 2013). Through the thickness parameter required for HUXt setup, which initialises the radial extent of the inserted CME structure, the subsequent deceleration rate of a CME can effectively be changed, essentially by altering the momentum of the CME (Owens, Lockwood, & Barnard, 2020). A CME of zero thickness is a spherical perturbation, whilst larger values produce more of a ”sausage” shape. In the version of HUXt used in this study (Version 1.0.0), the CME shape is limited to resolution of the grid cells within the model; longitudinally 2.8° and radially 1.5 $R_{\odot}$. In order to track the CME disturbance through the model, the edge of a CME is defined as where the velocity difference per a grid-cell is greater than 20km^{-1} than compared to the ambient (i.e. no CME) solar wind solution.

2.3 Ghost Fronts

To bring out dynamic features in HI images, it is common practice to take a running-difference of the images, wherein the previous image is subtracted from the current one to reveal finer detail. In doing so, static and slowly varying features are removed and any changes between HI images appear as bright (increased intensity) and dark (decreased intensity) features. A bright feature that forms a coherent shape is classified as a front. Two nearly identical leading CME fronts are frequently observed in such HI images that are separated by a few degrees of elongation (Scott et al., 2019). Such a feature is also seen for the December 12th 2008 CME, as shown in figure 2.

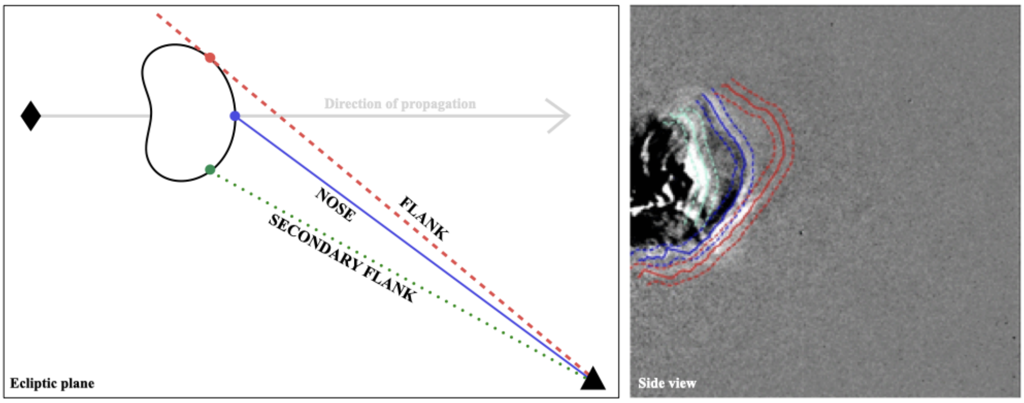

Figure 2. a) Schematic of the CME leading edge features that are detectable in Heliospheric Imager data using the ghost-front theory of Scott et al. (2019). Red dashed line shows the flank (i.e. tangent) of the CME edge, blue solid line shows the nose of the leading edge and pale green dotted line shows the position of a secondary flank. The position of a spacecraft, such as STEREO, is represented by the triangle and the Sun is positioned at the diamond. b) An example of a running-differenced Heliospheric Imager image taken from STEREO-B on December 13th 2008. The Sun is position on the left of the image and the Earth is positioned on the right. The fronts have been highlighted, where solid line is the average and dashed line is the uncertainty. The colour of the front corresponds to the feature colour in the schematic. Red is the outer most front, followed by blue and then pale green closest to the Sun.

It has been shown that there can be a correspondence between the position of the outer front and the pile up of plasma ahead of the CME (Pant et al., 2016). Shock fronts are produced when the speed of a CME eruption is significantly greater than the ambient solar wind, however, there are occasions where a ghost-front is observable but there is no in-situ evidence of a leading shock. The CME of 12 December 2008 (Scott et al., 2019) is one such example. It is also possible that multiple CME fronts observed in HI data represent different structural features of the same CME, for example the upstream disturbance, the leading edge and the flux rope (Möstl et al., 2011; Davis et al., 2009).

More recently Scott et al. (2019) demonstrated that for the December 12th CME, where the two fronts contained similar latitudinal structure in HI images, the fronts were consistent with the location of the leading edge (or 'nose') and flank of a single CME front.

Thomson scattering is vital in being able to understand how CMEs are seen in HI images. The intensity of scattered light in each pixel of an HI image is proportional to the density of free elections integrated along that line of sight as a function of distance from the observer. Features can therefore appear bright in an HI image for a number of reasons. For example, the nose of the CME, where the CME front lies along the line of propagation, is likely to appear bright because of the localised increase in plasma density. The tangent to the leading edge (i.e. the flank of the CME) can also appear bright due to the cumulative plasma density integrated along the extended line of sight. Thus two bright fronts can often be seen in HI images, each resulting from light scattered from different regions of the same front. This 'ghost front' model has been applied in the work of Chi et al. (2021) to simulate bright features within CME images. It was shown to be consistent with observations over a range of latitudes. This suggests that measuring the elongation difference between ghost fronts can help us determine the longitudinal shape and/or width of a CME from a single spacecraft. Further, there has been a suggestion that using both the nose and the flank to optimise HI-1 fitting could improve forecasting abilities of CMEs at L1/ Earth (Barnard et al., 2020; Hinterreiter et al., 2021).

3 Case study: December 12th 2008 CME

In COR1, the CME was first observed at a radial distance of 7.9 $R_\odot$ at 10:37 UTC December 12th 2008. Later the event was also captured by HI-1, first at a radial distance of 34 $R_\odot$ at 20:49 UTC and was tracked throughout the instrument's field of view. Many techniques have been developed to reconstruct CMEs using coronagraph data, such as the CME Analysis Tool (CAT) used by SWPC (Millward et al., 2013), geometric localisation (Koning et al., 2009), and equal masses (Colaninno & Vourlidas, 2009). By averaging these methods, Scott et al. (2019) concluded that this CME propagated along a solar longitude of 10 $\pm$ 4° and latitude 9 $\pm$ 2° (HEEQ coordinates) with a speed of 380 kms^{-1} whilst close to the Sun. Further, CME reconstruction using HI-1 data suggested an increased radial speed of 497 $\pm$ 63 km s^{-1} throughout the distances observed.

This CME was tracked though the HI-1 field of view using the same interface as used with Solar Storm Watch (Barnard et al., 2017). By identifying bright fronts within an image and taking the radial distance of these features where they cross the ecliptic plane, the elongation angle of each feature was measured. After repeating this for all HI images, a time-elongation profile was produced. We can see the time-elongation profiles for the features of the December 12th 2008 CME in figure 5a, where two fronts were identified in STEREO-A data and three-fronts from STEREO-B. These profiles were also included in the work by Scott et al. (2019), however only two features were identified within STEREO-B's HI images due to a limitation on the number of features that could be tracked at that time. Now, we find the "inner front" (shown in blue) to have a less-noisy time-elongation profile, similar to the profiles seen by STEREO-A. A third feature (shown in green) has not been used or identified in other ghost-front studies, but could plausibly be explained by one of the other multiple front theories mentions earlier. Hence, here in this work we do not use the time-elongation profile of the third front in our analysis. However, we do investigate if an extension of the ghost-front theory can explain this feature.

From ACE data, seen in figure 3, we analyse the CME's arrival at Earth. We interpret the enhancement in ion density at 07:00 UTC $\pm$ 1 hour on the December 16th 2008 as the arrival of the compressed solar wind ahead of the CME, just under four days from the first COR observation. Upon the arrival of the CME the solar wind velocity increases, seeing the value ranging from approximately 330kms^{-1} at arrival to 370 kms^{-1}

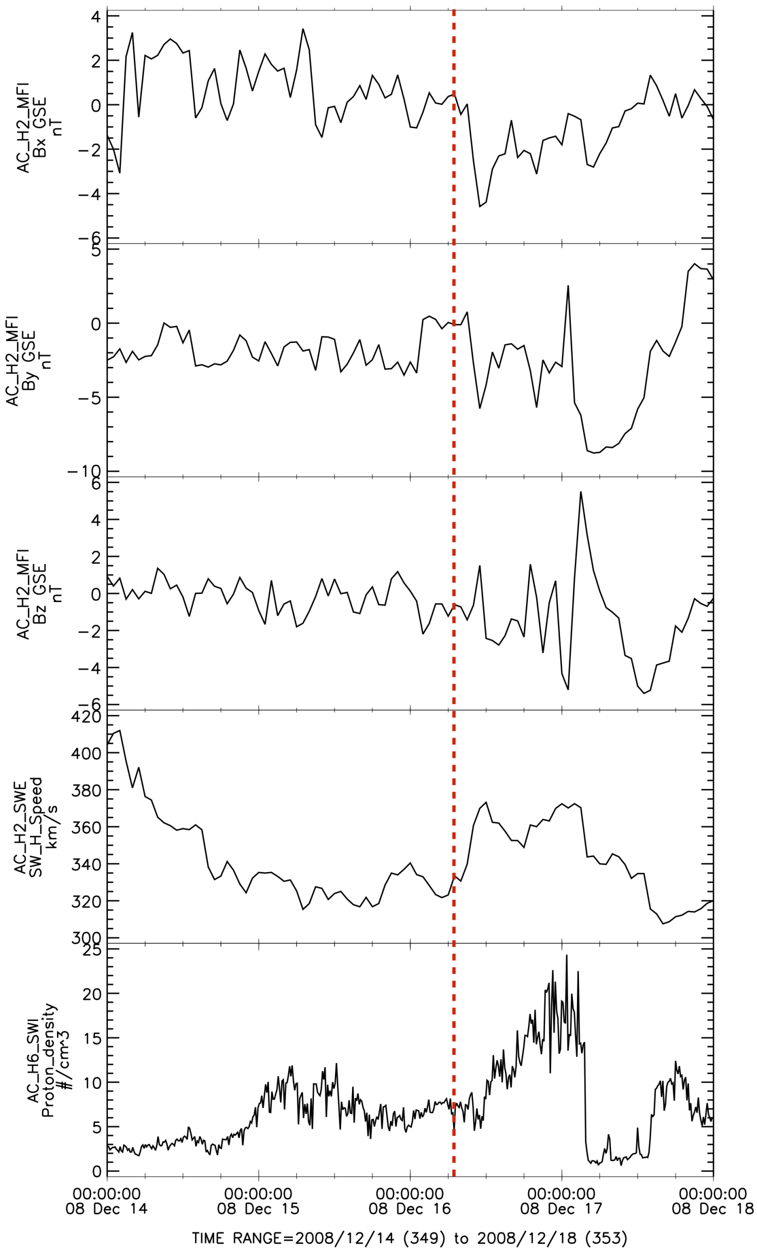

Figure 3. Solar wind data from NASA's ACE spacecraft. Top three panels show the heliospheric magnetic field (in GSE coordinates) and the lower two panels show the solar wind radial speed and proton concentration. The red dashed vertical line highlights the CME arrival time, as estimated from an enhancement in ion density. (Source: https://cdaweb.gsfc.nasa.gov/cgi-bin/eval1.cgi.)

several hours later, along with an associated enhancement in ion density. It becomes clear that these features are indeed associated with a CME when, a few hours later, the magnetic field turns southwards indicating the arrival of the magnetic structure. This observed arrival time is consistent with other studies (Davis et al., 2009; Deforest et al., 2013; Zhang et al., 2019).

4 Method

4.1 CME propagation ensemble

For the CME of December 12th 2008, a deterministic run of the HUXt model initialised with MAS solar wind data for CR2077 and CME initial conditions (42° width, 497 kms^{-1} speed, 10° longitude and 9° latitude), determined from STEREO COR observations, produces time-elongation profiles for the nose and the flank of the CME that are in reasonable agreement with the observations and result in an arrival time at Earth that is within 5.5 hours of the in-situ spacecraft observations. While this could be considered to be a successful result, it does not explore the sensitivity of the model to the uncertainty and accuracy of the initial solar wind and CME input data.

In this study, we investigate whether alterations can be made to the HUXt model to better reproduce the HI observations and whether such improvements in turn improves the model's ability to reproduce the observed CME arrival time at L1. To do so, 201-member (200 random and 1 deterministic member) ensembles of the HUXt model were made for a range of initial conditions that either saw alterations to the solar wind conditions or the CME parameterisation, each one called an experiment. For each experiment, the initial conditions of the modelled CME were perturbed using a random, uniform distribution corresponding to the uncertainty in observations. The modelled time-elongation profiles of the CME nose and flank were extracted from each model run by identifying where the CME front crossed the radial line of propagation (the nose) and the maximum observed elongation of the front from the position of each spacecraft (the flank). The combined nose and flank profiles as seen from both spacecraft simultaneously were used to determine the efficacy of each model run by computing the Root-Mean-Square-Error (RMSE) between model and observations. In this way, the model runs within each experiment can be ranked according to RMSE. By determining the relation between RMSE and arrival time error (ATE), we can determine if the HI observations contain any information that could be used to improve the estimated arrival time at Earth. We repeat the analysis using the flank only, similarly to the work of Barnard et al. (2020), to assess the benefit from using ghost fronts to evaluate model performance.

Three alterations to the HUXt model setup were considered as variable that could impact the model's outcome; the use of data assimilation to the MAS solar wind scheme; the location of the model inner boundary (30 $R_\odot$ compared with 8 $R_\odot$); and the magnitude of the assumed uncertainties in the initial CME observations. By taking combinations of these model alterations, a total of five experiments are presented here:

1. CME initialised with the parameter uncertainty estimated from COR observation, interacting with BRaVDA solar wind solution from 30 $R_\odot$.
2. CME initialised with twice the parameter uncertainty estimated from COR observation, interacting with BRaVDA solar wind solution from 30 $R_\odot$.
3. CME initialised with the parameter uncertainty estimated from COR observation, interacting with BRaVDA solar wind solution from 8 $R_\odot$.
4. CME initialised with twice the parameter uncertainty estimated from COR observation, interacting with BRaVDA solar wind solution from 8 $R_\odot$.
5. CME initialised with the parameter uncertainty estimated from COR observation, interacting with MAS solar wind solution from 30 $R_\odot$.

The initial condition values, associated uncertainty, and solar wind scheme used in each experiment can be found in table 1.

Table 1. Overview of initial conditions variables used for each experiment. Value and uncertainty (if applicable) of the inner boundary radial distance, CME speed, CME source location, CME full width, CME thickness, Earth's Carrington longitude at the start of the experiment and the solar wind scheme are displayed.

Model Run Name	**Inner Boundary ($R_\odot$)**	**Speed (kms^{-1})**	**Longitude (°)**	**Latitude (°)**	**Width (°)**	**Thickness ($R_\odot$)**	**Earth's Carrington Longitude**	**Solar Wind solution**
experiment 1	30	497 ± 63	10 ± 4	9 ± 2	42 ± 6	5 ± 2	67.966	BRaVDA
experiment 2	30	497 ± 126	10 ± 8	9 ± 4	42 ± 12	5 ± 4	67.966	BRaVDA
experiment 3	8	600 ± 150	10 ± 4	9 ± 2	42 ± 6	16.9 ± 2	63.363	BRaVDA
experiment 4	8	600 ± 300	10 ± 8	9 ± 4	42 ± 12	16.9 ± 4	63.363	BRaVDA
experiment 5	30	497 ± 63	10 ± 4	9 ± 2	42 ± 6	5 ± 2	67.966	MAS

In the following section, the reasoning behind the choice of each of these experiments will be considered in more detail.

4.2 Reducing the inner boundary of the model

CMEs have been shown to be accelerating in the initial stages of the propagation up to distances greater than 30 $R_\odot$ (Manchester et al., 2017). The acceleration is not primarily due to the interaction with the ambient solar wind, but, the CME's magnetic energy within the flux-rope driving it forward up to 20 $R_\odot$ (Subramanian & Vourlidas, 2007). The HUXt model does not account for such CME acceleration, but as the inner boundary is typically taken to be 30$R_\odot$, as is the case with the MAS model, this is not a major issue. However, injecting a CME with a geometrically simple shape into the model at 30 $R_\odot$ does not account for any distortion the CME may have undergone while propagating out from the initial coronagraph observations (at 8 $R_\odot$ where the CME appears to have a more regular structure). With the lack of magnetic field in HUXt CMEs (or other representations of cone model CMEs), it is important to ensure the kinematics of a CME in the earlier stages of propagation are represented by other means when using a lower inner boundary.

Firstly, in order to initialise the ambient solar wind at 8 $R_\odot$, the solar wind must be back-mapped to this location from the 30 $R_\odot$. We must consider changes in solar wind acceleration and solar longitude, resulting from solar rotation during the transit time, T, taken for this radial movement to occur between the two boundaries. Riley and Lionello (2011) stated a solar wind acceleration term based on MHD simulations as

$$accV(r) = \alpha V_0 \left[1 - exp\left(\frac{-(r - r_0)}{r_H}\right)\right], \tag{1}$$

where an acceleration term $\alpha = 0.15$ and the scale height r_H= 50 $R_\odot$ produced results in agreement with the HelioMAS model. This equation is used to compute V(8 $R_\odot$) from V(30 $R_\odot$). T is then given by

$$T = \int_{8R_\odot}^{30R_\odot} \frac{1}{V} dr, \tag{2}$$

where:

$$V(r) = V_0 + accV(r). \tag{3}$$

Using the information derived from these above equations, the change of solar longitude, $\Delta\phi$, can be calculated by

$$\Delta\phi = 2\pi \frac{T}{T_{syn}}, \tag{4}$$

where T_{syn} is the sidereal rotation period of the Sun. Since a structured solar wind is used, there are a range of different transit times and hence longitudinal changes between 30 $R_\odot$ and 8 $R_\odot$. This back-mapping method ignores any stream interaction that take place. The final step in the process interpolates the output on the HUXt's longitudinal grid spacing.

A cone CME will also alter in size significantly between these radial distances, whereby the CME radius will increase as the event expands throughout its propagation. As a result of the CME radius being smaller at a lower inner boundary, we must conserve the momentum of the event which can be done through the thickness parameter. Ultimately, we aim to simulate a CME from 8 $R_\odot$ that will obtain similar parameters at 30 $R_\odot$ to those we used to initialise the model at the same radial distance. To ensure the total radial extent of the CME is kept constant then the following equation must be true

$$2r_{30} + T_{30} = 2r_8 + T_8 \tag{5}$$

where r is the CME radius of the spherical ends and T is the thickness, together making the initial "sausage" shape of the CME, and the subscript tells us the initial height of the CME. With a reduced CME radius at 8 $R_\odot$, we require a greater initial thickness than seen at 30 $R_\odot$ to compensate. The radius of the spherical ends can be calculated using

$$r_{cme} = R_{cme} tan(\theta) \tag{6}$$

where R is the initial height of the CME and θ is the half-width angle of the CME. By substitution, we can find the equivalent thickness of the CME at the lower inner boundary using

$$T_8 = 2R_{30} tan(\theta) + T_{30} - 2R_8 tan(\theta). \tag{7}$$

For the December 12th 2008 event, we calculate that for a CME launching from 8 $R_\odot$ with half-width of 21° a thickness of 16.9 $R_\odot$ is required.

Since we cannot model the initial CME acceleration with HUXt, we simulate this CME acceleration by initialing the model with a speed greater than observed at 30 $R_\odot$ when using a lower inner boundary. Using CME parameters estimated from chronograph observations, a small set of runs was carried out in which only the initial CME speed is changed between runs. After exploring a large range of initial speeds (300 – 1200 kms^{-1}), a local minimum in RMSE for HI-1 measurements is found to occur at approximately 600 ± 100 kms^{-1} for all features tracked. Hence, we use this value to define the CME initial speed at the 8 $R_\odot$ boundary. The model runs continue to use COR observations made at the radial distance of this lower boundary to describe the source location and longitudinal width of the CME.

Finally, we want to test if the quoted uncertainties of the coronagraph fit were adequate for capturing all potential outcomes. We allow the ensemble members to perturb are the given uncertainty and twice the given uncertainty, still with a random, uniform distribution.

5 Results and Discussion

5.1 Modelling the solar wind: BRaVDA or HelioMAS?

We explore the differences of using HUXt with and without data assimilation of the in-situ solar wind observations by comparing the deterministic outcome of the model in each case. Earlier, we described the differences between the two solar wind schemes from the near-Earth solar wind speed time-series, however no CME was present in this case. Here, we initialise the CME using the estimated coronagraph observations for a 30 $R_\odot$ inner boundary. In figure 4 we can compare the impact of using data assimilated solar wind scheme using the geometric shape of the CME two-days into the propagation and the time-elongation profiles for the nose and flank.

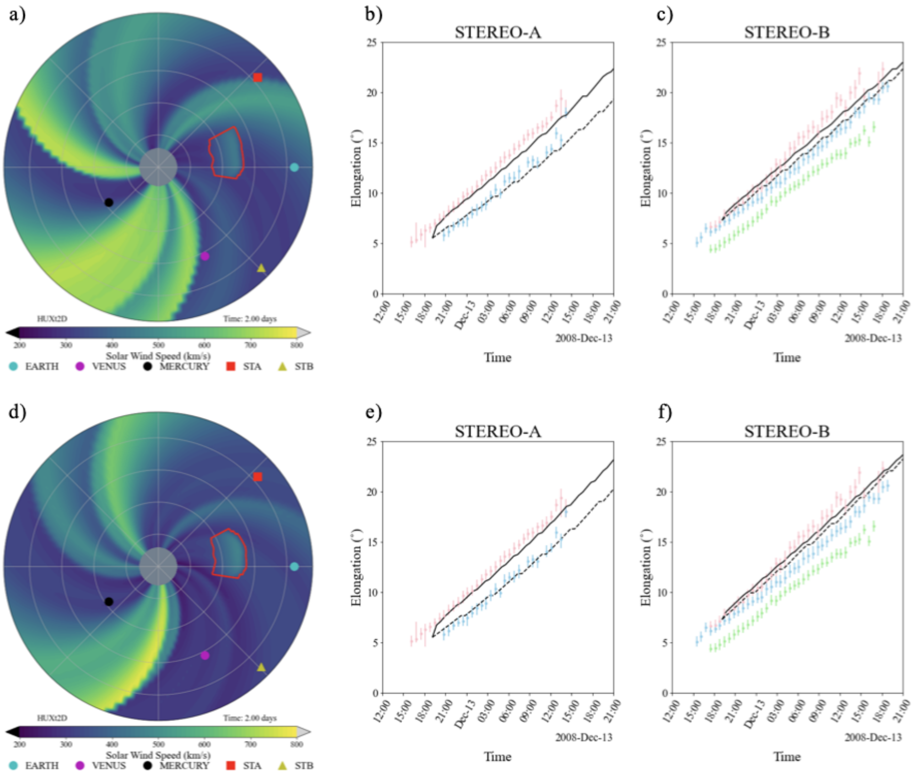

Figure 4. Comparison of HUXt output when ran with different solar wind schemes. The top panel shows the results from the MAS non-data assimilated solar wind scheme. The bottom panel shows the results from the BRaVDA data assimilated solar wind scheme. Ecliptic plane plot are displayed in a) and d), showing a CME's interaction with the solar wind structure two-day into simulation. Structured solar wind is shown by the background colour, whilst the CME edge is identified by the red-outlined shape. Markers for Earth, STEREO, Venus, and Mercury positions are also included. Time-elongation plots measured from the position of STEREO-A [b) and e)] and STEREO-B [c) and f)] show the evolution of the leading edge nose (black dashed) and flank (black solid) throughout the Heliospheric-Image 1 field of view. Coloured error bars show the HI-1 data.

When the MAS (non-data assimilated) solar wind scheme is used, we find that the time-elongation profile of the nose and flank throughout the HI-1 field of view agree well with STEREO-A observation, obtaining a combined RMSE of 0.913°, and STERE0-B, obtaining a combined RMSE of 0.809°. From both spacecraft, the RMSE value is 0.856°. This CME hindcast has an L1 arrival of 12:30 UTC ± 34 minutes on December 16th 2008 (5.5 hours after observed arrival) with a speed of 328 kms^{-1}.

Alternatively, using BRaVDA to assimilate in-situ observations we find that the CME hindcast has an estimated arrival time at Earth of 07:53 UTC ± 34 minutes on the same date. This hindcast provides an estimated arrival time that is 4.62 hours earlier than MAS, and is within the observed arrival time uncertainty (07:00 ± 1.0 hour on the December 16th 2008). Further, we find that the CME arrives with a speed of 353 kms^{-1}, which falls within the observed range of speeds seen in figure 3. Computing the RMSE of the time-elongation profiles, we find that by using BRaVDA we recreate the observed time-elongation profiles better from the viewpoint of STEREO-A (0.684°) but not from STEREO-B (0.929°). Due to the broader, faster stream seen in the HelioMAS solution at 12:00 UTC on the December 13th 2008 in figure 1, the CME evolution differs significantly enough whereby the westward flank (observed by STEREO-B) is dragged out with time causing a flatter leading edge to the CME, as seen in figure 4b. This produces an flank time-elongation profile with larger angles which the RMSE values suggest is more representative of the HI-1 observation. Despite this, when combining the viewpoint of both spacecraft, the BRaVDA solution still reduced the RMSE of the time-elongation profiles (0.830°), although marginal.

In this case study, neither solar wind scheme produced a solution with a significantly smaller RMSE than the other. But it is highlighted that understanding CME distortion cause by interaction with solar wind streams plays a vital role in accurately reproducing HI-1 observations. But since the BRaVDA scheme reduced the error in arrival time then we continue to use this solar wind scheme going forward with the study.

5.2 Constraining models using Ghost-Front features

In figure 5 we show a development of simulating time-elongation profiles that reasonably reproduce the profiles of tracked fronts within HI-1 imagery. In the top row we show the observed time-elongation profiles seen by STEREO's Heliospheric Imager-1 (more details of these plots was included in section 2.3), and in the middle row we show all HUXt simulated profiles from the 201-member ensemble of experiment 1 (modelling CME from 30 $R_\odot$ with parameters varying within coronagraph observed estimates; table 1) overlaid with the HI-1 observations. We show the feature identified as the flank in red and the nose in blue, directly relating to the colours seen in the top row. The bold line indicates the deterministic run. From this ensemble, we show the best-fit time-elongation profile for the nose and flank as seen from both STEREO spacecraft - i.e., the model run that produced the lowest RMSE - in the bottom row. From the perspective of STA, the modelled profiles agree with the front elongations fairly well (0.598° RMSE). The flank appears to fit very well, with the simulated profile agreeing within the error of the HI-1 observed fronts, meanwhile, the nose feature doesn't perform quiet as well. However the gradient of these features is in good visual agreement. On the other hand, from the perspective of STB, the separation between the nose and flank is narrower than seen in the observations. Here we see that the gradient of the flank's time-elongation profile is less than observed, with many of the observations differing from the simulations by more than can be explained by uncertainties. The model nose elongation agrees with the points better and therefore we find a RMSE of 0.752°. Collectively, this model run agrees with the observations with a RMSE of 0.688°.

Here, we can also introduce the third feature seen by STEREO-B (shown in green in figure 5). This appears to correspond to the location of the CME flank observed from STEREO-A, as seen from STEREO-B. This may be due to the proximity of this flank to STEREO-B resulting in a bright feature. Using this interpretation, the observations match the modelled location of this feature (0.556° RMSE) highlighting a good fit. Whilst this is interesting to note, and may help identify the cause of this feature in the images, it is not used further in the analysis presented in this paper, since it is unclear how frequently such features would appear in other case studies.

The narrower difference between nose and flank time-elongation profiles produced by the model suggests that the model is not capturing the CME distortion accurately enough. More precisely, the radius of curvature of the CME front is too small. One ex-

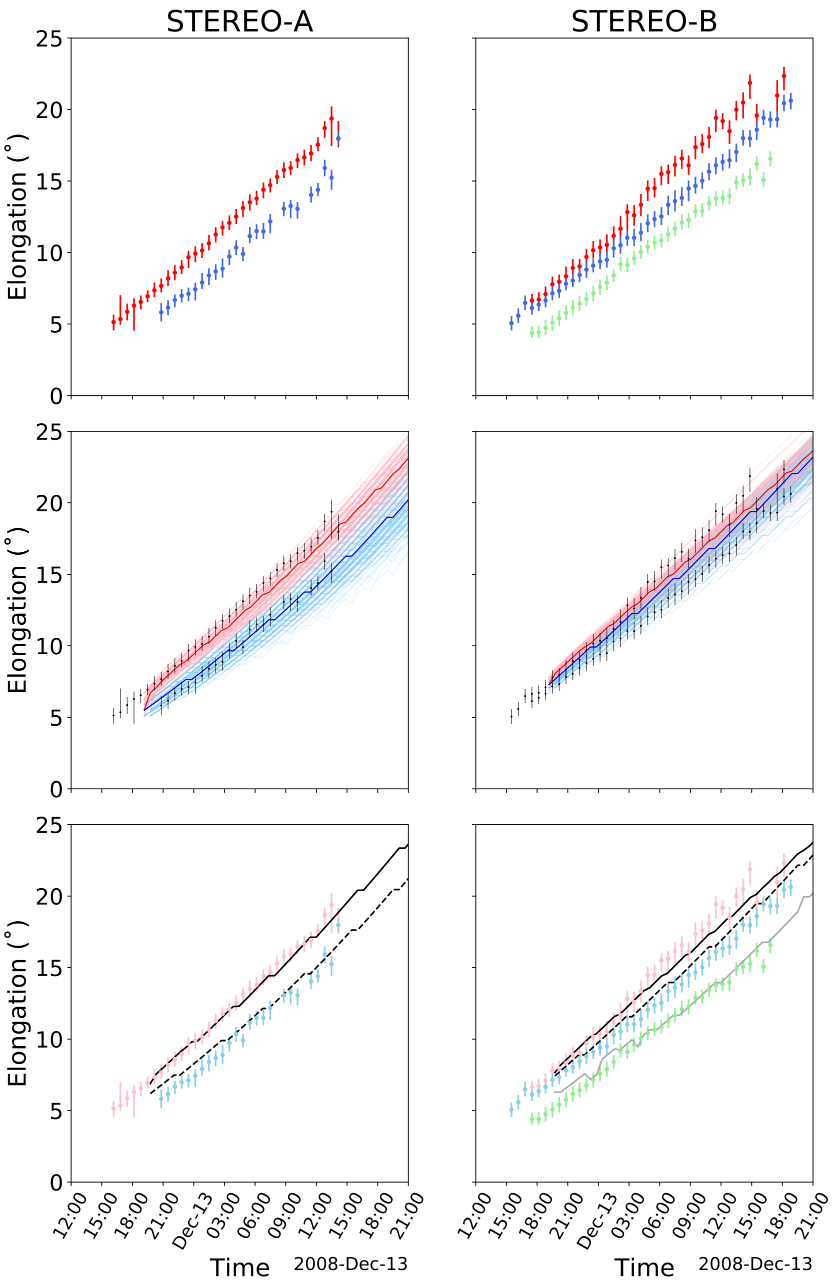

Figure 5. Time-elongation profiles for experiment 1, with HUXt modelling CME propagation from 30 $R_\odot$ inner boundary, measured from the position of STEREO-A (left column) and STEREO-B (right column). Top row: error bar profiles of the dense-plasma fronts seen in Heliospheric Imager data, measured using the Solar StormWatch technique. Middle row: Modelled data showing the profiles of the nose (blue) and flank (red) from the 201 member ensemble, with the deterministic run shown in bold. Bottom row: profiles of the best-fit run, i.e. the minimised RMSE error of the nose and flank from both spacecraft. Here, we also show the profile of the secondary flank in solid grey in STEREO-B only.

planation could be that we have used an insufficient range over which the initial parameters of the CME were allowed to vary in the ensemble. We later test this by allowing the initial CME conditions to vary by up to twice the quoted parameter uncertainties. Another reason could be that significant distortion of the CME occurs before 30 $R_\odot$. Despite this "best-fit" model run agreeing with the HI observation better than the deterministic run, we find that we obtain an arrival time that is 2 hours 18 minutes earlier and falls outside the observed uncertainty. Such result demonstrates the limitation of using HI time-elongation profiles to constrain a CME's evolution as they are essentially degenerate for many combinations of initial CME parameters. So, as you find here, the "best fit" time-elongation profile might correspond to a simulation that poorly reflects the arrival time at Earth.

Further, due to the random nature of the sampling, identifying the experiment member that produces the lowest RMSE may not representative of the entire ensemble, and as such it is not sufficient to use this to draw conclusions on the benefit of using ghost fronts to constrain propagation modelling. Hence we now explore the correlation between the HI-1 elongation RMSE and arrival time error, as shown in figure 6 for the experiments modelled from a 30 $R_\odot$ inner boundary. We note that there are two data clusters for experiment 1 (fig 6a) of which both appear to form a local minimum at similar arrival time error, though one has much higher RMSE values. The cause of the two clusters is yet to be determined, but a plausible explanation is that there is a common sensitivity to one of the initial values between these model runs. For example a wider or narrower CME can produce time-elongation profiles that are off-set from the observations by a few degrees yet the propagation of the nose is not impacted and hence produces an arrival time in agreement with other members. By finding a subset of ensemble members which identify the members with lowest RMSE value, we can ensure that we only consider those ensemble members that best match with the HI-1 data.

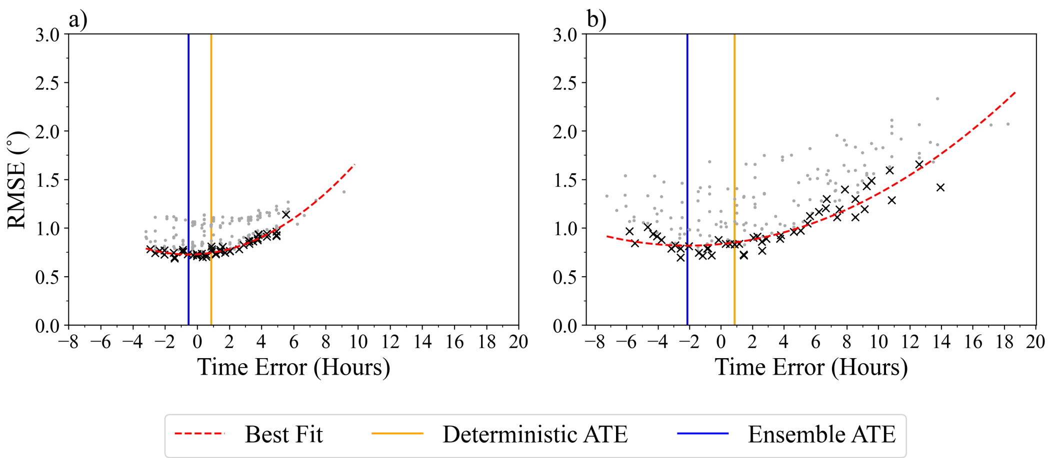

Figure 6. Scatter plots of time-elongation profile RMSE values against arrival time error for each model member. In these experiments, HUXt is configured with an inner boundary of 30RS with initial conditions allowed to vary with (a) the coronagraph estimated uncertainty and (b) twice the estimated uncertainty. A quadratic line of best fit (red, dashed) is fit to the lowest 25% of data per a bin (black dots).

To do this, we bin the members by their ATE, with 34 minute resolution (HUXt's output time-step in the configuration of this study), to ensure the ensemble distribution continues to be represented. The lowest 25% of data points per each bin are then found and used to create the data subset in which the regression line is best fit to. By taking the subset of data like this, we can explore the variation of best-fit RMSE as a function of arrival time while accounting for the noise generated by random sampling of the CME initial conditions. Hence, upon calculating the minimum value of the curve we can analyse the relationship between the quality of fit and the arrival time at L1. The uncertainty of the fit and is measured by where the line of best fit is significantly different from the minimum value, based on 1 standard deviation error. In such way, sharp curves that better define the minimum will have a low uncertainty whilst less well defined curves have greater uncertainty.

For experiment 1, the scatter produces a curve minimising at -0.5 ± 0.2 hours which equates to an arrival time before the observed arrival. This is within the observed arrival uncertainty of ± 1.0 hours. The result is 1.5 hours before the deterministic hindcast, but since this is only a difference of three model resolution time-step we cannot say that this is a strong improvement on the deterministic hindcast by. The RMSE value associated with the curve minimum in 0.726°. We carry out the same analysis for experiment 2, where the ensemble of CME parameters are generated by randomly sampling from uniform distributions with twice the spread of experiment 1. We find that the RMSE variation minimises at -2.1 ± 0.5 hours. This result produces a less accurate arrival time than both the deterministic and experiment 1 model runs, which is suggested by an insignificant change to the minimising RMSE value of 0.818°, highlighting no benefit for doubling the range over which the CME initial conditions are allowed to vary. From increasing the initial parameter range and maintaining the ensemble size, we note that there is a reduced resolution within the parameter space which may increase the variation in RMSE values between ensemble members.

If only the flank time-elongation profile (i.e. the outermost CME front detected in HI) is considered, as was done in the work by Barnard et al. (2020), we find that the quadratic curve minimises at -4.4 ± 1.1 hours with RMSE of 0.900° for experiment 1 and -11.1 ± 4.9 hours with RMSE of 0.697°for experiment 2. However, we note these ATE values fall outside of the range of values obtained by the ensemble members (minimum ATE is 03:48 UTC December 16th 2008 and 23:44 UTC December 15th 2008 respectively) highlighting that the outcomes are likely to be unreliable estimates. Thus far in the case study, an early CME arrival is estimated when launched from an initial height of 30 $R_\odot$, but the accuracy of the ATE estimate is improved when including CME nose tracking in ensemble modelling.

Table 2. Overview of the arrival time error results of the experiments. Deterministic value is computed using a single fun of HUXt initialise with the COR-1 parameter estimates. Ensemble (Ens.) ATE is the minimum of the quadratic relation between the HI-1 elongation RMSE and arrival time error for the lowest 25% of members, as seen in figure 6 and 7. Where the number is in bold font, we note that the value falls outside of the ensemble range of ATE values.

Model Run Name	**Deterministic ATE (hours)**	**Nose and Flank Ens. ATE (hours)**	**Flank Ens. ATE (hours)**
Experiment 1	0.9 ± 0.6	-0.5 ± 0.2	**-4.4 ± 1.1**
Experiment 2	0.9 ± 0.6	-2.1 ± 0.5	**-11.1 ± 4.9**
Experiment 3	0.4 ± 0.6	2.8 ± 0.5	0.7 ± 0.8
Experiment 4	0.4 ± 0.6	2.9 + 0.6	1.6 ± 1.0
Experiment 5	5.5 ± 0.6	n/a	n/a

5.3 Lowering the model inner boundary to 8 $R_\odot$

By reducing the inner boundary to the radius at which the parameters were estimated, the deterministic hindcast produces an L1 arrival at 07:24 UTC + 34 minutes on the December 16th 2008 with a speed of 333 kms^{-1}. Compared to 30 $R_\odot$ deterministic, the difference in arrival time estimate is smaller than the model resolution, therefore, we can say the model output performs similarly. When comparing the time-elongation profiles of the nose and flank to the fronts observed in HI-1, the RMSE values for STA, STB, and both spacecraft are 0.611°, 0.741°, and 0.688° respectively. This equates to an improvement in the RMSE compared with the 30 $r_\odot$ deterministic run by at least 10%.

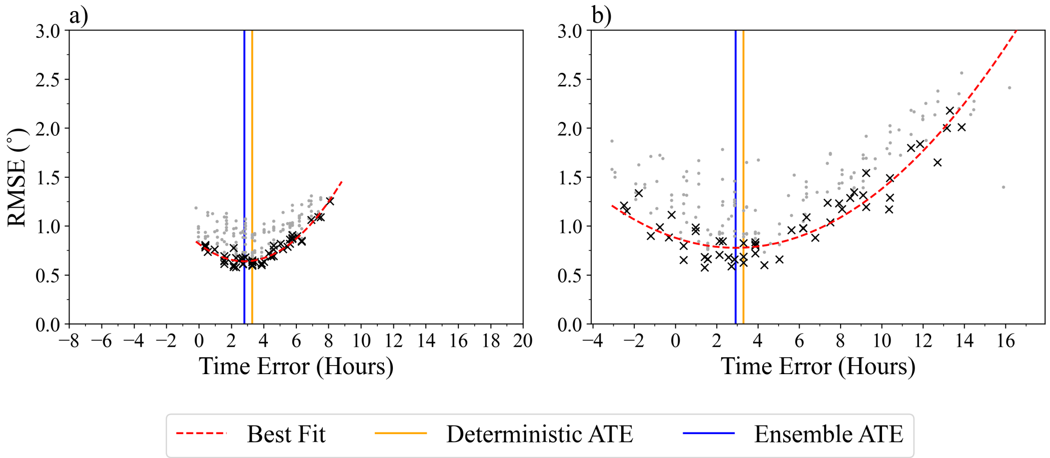

Figure 7. Scatter plots of the time-elongation profile RMSE values and the arrival time error for each model member in (a) experiment 3 and (b) experiment 4. A quadratic line of best fit (red, dashed) is fit to the lowest 25% of data per a bin (black dots).

We analyse the model outputs for experiment 3 and 4 and display the relationship between the RMSE and ATE in figure 7. By fitting the curve to the lowest 25% of binned data, we find that the curve minimises at 2.8 ± 0.5 hours and 2.9 ± 0.5 hours for experiment 3 and 4 respectively. There is no improvement to the arrival time accuracy produced here by both experiments than compared to those already discussed, and we find that the estimates now predict an arrival later than observed. But it is interesting to see that despite doubling the range over which the initial parameters can vary in experiment 4, the fit to the data produces a consistent ATE result. This was not observed in the earlier experiment suggesting that by simulating early distortion to the CME then the time-elongation profiles throughout the HI-1 field of view is more unique to the model member allowing RMSE values to better indicate the performance of the initial parameters. We see this demonstrated in the figure by a sharper best-fit curve fitting to the data than compared to their counterpart experiment for 30 $R_\odot$.

The 8 $R_\odot$ ensemble estimated ATE associates with a lower RMSE value than its 30 $R_\odot$ counterpart. 0.726° drops to 0.638° when using the estimated coronagraph parameter uncertainty (experiment 3), and 0.818° drops to 0.776° when using twice the estimated uncertainties (experiment 4). These results highlight again that by allowing the CME to distort before reaching the field of view covered by HI-1 then the model can simulate the real data with better accuracy. Whilst this is expected of a real CME propagation thought the heliosphere, it is important to note that the simplified HUXt model is replicating the kinematics.

Again, we look at the results for a situation where only the flank RMSE is considered. It is found that the curve minimises at 0.7 ± 0.8 hours for experiment 3 and 1.6 ± 1.0 hours for experiment 4, therefore producing a better estimate of the arrival time than using both the nose and flank features. Whilst previous results highlight that the elongation of multiple fronts detected in HI-1 data can be replicated using the nose and flank of a CME leading edge, these results here suggest that tracking a single feature may also be sufficient in producing arrival predictions as long as we account for early CME distortion by lowering the inner boundary of the model. The accuracy with which the flank's time-elongation profile evolves from the lower inner boundary may be unique to this case study in which HUXt accurately captures the distortion of a relatively slow-moving event.

6 Conclusions

We have modelled the December 12th 2008 CME using the HUXt solar wind model with BRaVDA's solar wind solution to produce multiple ensemble hindcasts. The data assimilated solar wind scheme was found to improve the arrival time error of the deterministic run by 4.62 hours, and produced an estimated arrival time that coincided with the observed CME arrival at L1 on December 16th 2008, 07:00 UTC ± 1.0 hour. Each experiment investigates the sensitivity of model inner boundary and the parameter uncertainty using a 201-member ensemble, and a collective L1 arrival time error is estimated based upon the relationship between the RMSE of HI-1 observation of the nose and flank and arrival time error of the individual members.

From the presented results, it is clear that accounting for CME distortion, at altitudes below the typical lower boundary of solar wind models, is vital for accurate modelling. We have shown here that this can be achieved by two methods. Firstly, we can use the multiple fronts seen in HI-1 images to inform us of the longitudinal distortion. By tracking the nose and flank of the CME we can evaluate the model's performance against the time-elongation profiles of the ghost-front features observed by HI images. Allowing the ensemble parameters to vary within the uncertainty of chronograph parameter estimates, we were able to obtain an quadratic function that estimates an L1 arrival time within one-hour before the observed arrival. If only the flank was used then the same experiment the result was unrealistic, producing an ATE which fell outside the ensemble's range. Alternatively, we can lower the model inner boundary to allow distortion to the CME shape before reaching the HI-1 field of view. In doing so, RMSE values of the ensemble members are more varied such that we obtain lower RMSE values via this method, suggesting the time-elongation profiles better represent the model's sensitivity to the initial conditions. The hindcast estimate is less accurate than method one (approximately 3 hours after observed arrival), however the ATE is consistent despite allowing ensemble parameters to vary within 1x and 2x the uncertainty of chronograph parameter estimates. On this occasion, evaluating model performance based on the CME flank profile not only worked but also estimated a better L1 arrival time error, producing an arrival error of no more than 1.6 ± 1.0 hour. But this was associated to largest RMSE values of all the work presented. Upon investigating the efficacy of the uncertainty estimates associated with the CME characterisation from the data, there was no improve to the hindcast (in this example) suggesting that the uncertainties quoted for the CME initial conditions are indeed adequate. Since current magnetohydrodynamic forecast models use a heliospheric inner boundary of approximately 30 $R_\odot$, above which most CME acceleration is considered to have already occurred, adopting the tracking ghost-front features as a way of constraining forecast models would seem to be the most convenient way of accounting for low altitude distortion of the CME.

Through this research, we have highlighted the efficacy of the HUXt model, showing the ability to account for the missing physics (i.e., plasma is assumed to be purely radial to eliminate the need of complex magnetic equations to describe its motion), especially at a lowered inner boundary, to produce near-accurate estimated arrivals at L1 from the flank alone.

Of course, we have only looked at a single event in this study, which is of a slow-moving CME. Further investigations following this should explore whether these conclusions are consistent across a range of CME initial conditions and viewing geometries. For fast-moving events, which are more geoeffective, it is also necessary to differentiate between ghost fronts and shock-fronts propagating ahead of the CME. Here we analysed results based upon observations from the twin spacecraft mission STEREO, whereas future missions like ESA's Vigil L5 Langrangian point (Vourlidas, 2015; Akioka et al., 2005) will only provide a HI viewpoint from one position outside the Sun-Earth line. In the current event, our interpretation of the data suggests that a single spacecraft is able to detect three features of the leading edge (the CME nose and both flanks), suggesting that significant benefits to forecasting accuracy could be obtained using data from a single spacecraft using ghost front observations.

Using HI time-elongation profiles to assess the model performance of CME distortion can be limiting as they can be degenerate for many combinations of initial CME parameters. Therefore, estimating the arrival time using a function which describes the arrival time error and RMSE is more representative of the ensemble, removes noise produced from random sampling and allows us to analyse and the impact ghost-fronts. This would not be possible if we only seek the single member that produced the best-fit to HI-1 observations. Adopting a comprehensive systematic sampling approach (where model runs are created for all combinations of input parameters within their uncertainty intervals) would be computationally more expensive but may enable a consistent estimate of the best-fit to the ghost-front data. This will be considered in future work.

7 Data Availability

The HUXt model (version 1.0.0) used in the research can be accessed at https://github.com/University-of-Reading-Space-Science/HUXt. Data assimilated solar wind scheme BRaVDA can be access from https://github.com/University-of-Reading-Space-Science/BRaVDA, using MAS inputs from http://www.predsci.com/mhdweb/home.php. ACE data is accessible via https://cdaweb.gsfc.nasa.gov/cgi-bin/eval1.cgi. Heliospheric Imager data was accessed from http://www.ukssdc.rl.ac.uk/solar/stereo/data.html and analysed using the Solar Stormwatch front tracking interface.

Acknowledgments

We are greatful to the STEREO/HI instrument team at Rutherford Appleton Laboratory and the UK Solar System Data Centre for the creation and access to Heliospheric Imager data. We also thank the scientist and CDAWed who contributed to the creation and open access to ACE data. Further appreciation to the Solar StormWatch Team and Zooniverse who developed the front tracking interface which provided the time-elongation profiles essential to this work. L. A. James is funded through STFC studentship ST/T506370/1. C. J. Scott, L. A. Barnard and M. J. Owens are funded by STFC ST/V000497/1. M. J. Owens and M. S. Lang are funded by NERC NE/S010033/1.

References

Akioka, M., Nagatsuma, T., Miyake, W., Ohtaka, K., & Marubashi, K. (2005). The l5 mission for space weather forecasting. *Advances in Space Research*, *35*, 65-69. doi: 10.1016/j.asr.2004.09.014

Arge, C. N., Luhmann, J. G., Odstrcil, D., Schrijver, C. J., & Li, Y. (2004). Stream structure and coronal sources of the solar wind during the may 12th, 1997 cme. *Journal of Atmospheric and Solar-Terrestrial Physics*, *66*, 1295-1309. doi:

10.1016/j.jastp.2004.03.018
Arnoldy, R. L. (1971). Signature in the interplanetary medium for substorms. *Journal of Geophysical Research*, *76*, 5189-5201. doi: 10.1029/ja076i022p05189
Barnard, L. A., de Koning, C. A., Scott, C. J., Owens, M. J., Wilkinson, J., & Davies, J. A. (2017). Testing the current paradigm for space weather prediction with heliospheric imagers. *Space Weather*, *15*, 782-803. doi: 10.1002/2017SW001609
Barnard, L. A., Owens, M. J., Scott, C. J., & Koning, C. A. (2020). Ensemble cme modeling constrained by heliospheric imager observations. *AGU Advances*, *1*. doi: 10.1029/2020av000214
Billings, D. (1966). *A guide to the solar corona.* Academic Press.
Byrne, J. P., Maloney, S. A., McAteer, R. T., Refojo, J. M., & Gallagher, P. T. (2010). Propagation of an earth-directed coronal mass ejection in three dimensions. *Nature Communications*, *1*. doi: 10.1038/ncomms1077
Cane, H. V., & Richardson, I. G. (2000). Coronal mass ejections, interplanetary ejecta and geomagnetic sotrms. *Journal of Geophysical Research: Space Physics*, *27*, 3591-3594. Retrieved from `http://dx.doi.org/10.1016/j.jastp.2009.08.005`
Cannon, P. (2013). *Extreme space weather: impacts on engineered systems and infrastructures.* Retrieved from `http://www.raeng.org.uk/news/publications/list/reports/Space_Weather_Full_Report_Final.PDF`
Cash, M. D., Biesecker, D. A., Pizzo, V., Koning, C. A. D., Millward, G., Arge, C. N., … Odstrcil, D. (2015). Ensemble modeling of the 23 july 2012 coronal mass ejection. *Space Weather*, *13*, 611-625. doi: 10.1002/2015SW001232
Chao, J. K., & Chen, H. H. (2001). Prediction of southward imf bz. *Geophysical Monograph Series*, *125*, 183-189. doi: 10.1029/GM125p0183
Chi, Y., Scott, C., Shen, C., Barnard, L., Owens, M., Xu, M., … Lockwood, M. (2021). Modeling the observed distortion of multiple (ghost) cme fronts in stereo heliospheric imagers. *The Astrophysical Journal Letters*, *917*, L16. Retrieved from `http://dx.doi.org/10.3847/2041-8213/ac1203` doi: 10.3847/2041-8213/ac1203
Colaninno, R. C., & Vourlidas, A. (2009). First determination of the true mass of coronal mass ejections: A novel approach to using the two stereo viewpoints. *Astrophysical Journal*, *698*, 852-858. doi: 10.1088/0004-637X/698/1/852
Davies, J. A., Harrison, R. A., Perry, C. H., Möstl, C., Lugaz, N., Rollett, T., … Savani, N. P. (2012). A self-similar expansion model for use in solar wind transient propagation studies. *Astrophysical Journal*, *750*. doi: 10.1088/0004-637X/750/1/23
Davis, C. J., Davies, J. A., Lockwood, M., Rouillard, A. P., Eyles, C. J., & Harrison, R. A. (2009). Stereoscopic imaging of an earth-impacting solar coronal mass ejection: A major milestone for the stereo mission. *Geophysical Research Letters*, *36*, 1-5. doi: 10.1029/2009GL038021
Deforest, C. E., Howard, T. A., & McComas, D. J. (2012). Disconnecting open solar magnetic flux. *Astrophysical Journal*, *745*. doi: 10.1088/0004-637X/745/1/36
Deforest, C. E., Howard, T. A., & Tappin, S. J. (2011). Observations of detailed structure in the solar wind at 1 au with stereo/hi-2. *Astrophysical Journal*, *738*, 1-12. doi: 10.1088/0004-637X/738/1/103
Deforest, C. E., Howard, T. A., & Tappin, S. J. (2013). The thomson surface. ii. polarization. *Astrophysical Journal*, *765*. doi: 10.1088/0004-637X/765/1/44
Dungey, J. W. (1961). Interplanetary magnetic field and the auroral zones. *Physical Review Letters*, *6*, 47-48. doi: 10.1103/PhysRevLett.6.47
Eyles, C. J., Harrison, R. A., Davis, C. J., Waltham, N. R., Shaughnessy, B. M., Mapson-Menard, H. C., … Rochus, P. (2009). The heliospheric imagers onboard the stereo mission. *Solar Physics*, *254*, 387-445. doi: 10.1007/s11207-008-9299-0

Gosling, J. T. (1993). The solar flare myth. *Journal of Geophysical Research: Space Physics*, *98*, 18937-18949. doi: 10.1029/93ja01896

Hapgood, M., & Thomson, A. (2018). Its impact on earth and implications for business.

Henley, E. M., & Pope, E. C. (2017). Cost-loss analysis of ensemble solar wind forecasting: Space weather use of terrestrial weather tools. *Space Weather*, *15*, 1562-1566. doi: 10.1002/2017SW001758

Hinterreiter, J., Amerstorfer, T., Reiss, M. A., Möstl, C., Temmer, M., Bauer, M., ... Owens, M. J. (2021). Why are elevohi cme arrival predictions different if based on stereo-a or stereo-b heliospheric imager observations? *Space Weather*, 1-18. doi: 10.1029/2020sw002674

Holst, B. V. D., Sokolov, I. V., Meng, X., Jin, M., Manchester, W. B., Tóth, G., & Gombosi, T. I. (2014). Alfvén wave solar model (awsom): Coronal heating. *Astrophysical Journal*, *782*. doi: 10.1088/0004-637X/782/2/81

Howard, R. A., Moses, J. D., Vourlidas, A., Newmark, J. S., Socker, D. G., Plunkett, S. P., ... Carter, T. (2008). Sun earth connection coronal and heliospheric investigation (secchi). *Space Science Reviews*, *136*, 67-115. doi: 10.1007/s11214-008-9341-4

Howard, T. A., & Deforest, C. E. (2012). The thomson surface. i. reality and myth. *Astrophysical Journal*, *752*. doi: 10.1088/0004-637X/752/2/130

Howard, T. A., Tappin, S. J., Odstrcil, D., & Deforest, C. E. (2013). The thomson surface. iii. tracking features in 3d. *Astrophysical Journal*, *765*. doi: 10.1088/0004-637X/765/1/45

Iwai, K., Shiota, D., Tokumaru, M., Fujiki, K., Den, M., & Kubo, Y. (2021). Validation of coronal mass ejection arrival-time forecasts by magnetohydrodynamic simulations based on interplanetary scintillation observations. *Earth, Planets and Space*, *73*, 1-17. doi: 10.1186/s40623-020-01345-5

Kahler, S. (1987). Coronal mass ejections. *Reviews of Geophysics*, *25*, 663-675. doi: 10.1029/RG025i003p00663

Kaiser, M. L., Kucera, T. A., Davila, J. M., Cyr, O. C., Guhathakurta, M., & Christian, E. (2008). The stereo mission: An introduction. *Space Science Reviews*, *136*, 5-16. doi: 10.1007/s11214-007-9277-0

Koning, C. A. D., Pizzo, V. J., & Biesecker, D. A. (2009). Geometric localization of cmes in 3d space using stereo beacon data: First results. *Solar Physics*, *256*, 167-181. doi: 10.1007/s11207-009-9344-7

Lang, M., & Owens, M. J. (2019). A variational approach to data assimilation in the solar wind. *Space Weather*, *17*, 59-83. doi: 10.1029/2018SW001857

Lang, M., Witherington, J., Turner, H., Owens, M., & Riley, P. (2020). Improving solar wind forecasting using data assimilation. , 1-29. Retrieved from http://arxiv.org/abs/2012.06362

Lee, C. O., Arge, C. N., Odstrčil, D., Millward, G., Pizzo, V., Quinn, J. M., & Henney, C. J. (2013). Ensemble modeling of cme propagation. *Solar Physics*, *285*, 349-368. doi: 10.1007/s11207-012-9980-1

Linker, J. A., Mikic, Z., a Biesecker, D., Forsyth, R. J., Gibson, S. E., a J Lazarus, & Lecinski, A. (1999). during whole sun month. , *104*, 9809-9830.

Liu, Y., Davies, J. A., Luhmann, J. G., Vourlidas, A., Bale, S. D., & Lin, R. P. (2010). Geometric triangulation of imaging observations to track coronal mass ejections continuously out to 1 au. *Astrophysical Journal Letters*, *710*, 82-87. doi: 10.1088/2041-8205/710/1/L82

Lugaz, N., Hernandez-Charpak, J. N., Roussev, I. I., Davis, C. J., Vourlidas, A., & Davies, J. A. (2010). Determining the azimuthal properties of coronal mass ejections from multi-spacecraft remote-sensing observations with stereo secchi. *Astrophysical Journal*, *715*, 493-499. doi: 10.1088/0004-637X/715/1/493

Manchester, W., Kilpua, E. K., Liu, Y. D., Lugaz, N., Riley, P., Török, T., & Vršnak, B. (2017). The physical processes of cme/icme evolution. *Space Sci-*

ence Reviews, *212*, 1159-1219. Retrieved from http://dx.doi.org/10.1007/s11214-017-0394-0 doi: 10.1007/s11214-017-0394-0

Mays, M. L., Taktakishvili, A., Pulkkinen, A., MacNeice, P. J., Rastätter, L., Odstrcil, D., ... Kuznetsova, M. M. (2015). Ensemble modeling of cmes using the wsa–enlil+cone model. *Solar Physics*, *290*, 1775-1814. Retrieved from http://dx.doi.org/10.1007/s11207-015-0692-1 doi: 10.1007/s11207-015-0692-1

Millward, G., Biesecker, D., Pizzo, V., & Koning, C. A. D. (2013). An operational software tool for the analysis of coronagraph images: Determining cme parameters for input into the wsa-enlil heliospheric model. *Space Weather*, *11*, 57-68. doi: 10.1002/swe.20024

Möstl, C., Rollett, T., Lugaz, N., Farrugia, C. J., Davies, J. A., Temmer, M., ... Biernat, H. K. (2011). Arrival time calculation for interplanetary coronal mass ejections with circular fronts and application to stereo observations of the 2009 february 13 eruption. *Astrophysical Journal*, *741*. doi: 10.1088/0004-637X/741/1/34

Odstrcil, D. (2003). Modeling 3-d solar wind structure. *Advances in Space Research*, *32*, 497-506. doi: 10.1016/S0273-1177(03)00332-6

Oughton, E. J., Hapgood, M., Richardson, G. S., Beggan, C. D., Thomson, A. W., Gibbs, M., ... Horne, R. B. (2019). A risk assessment framework for the socioeconomic impacts of electricity transmission infrastructure failure due to space weather: An application to the united kingdom. *Risk Analysis*, *39*, 1022-1043. doi: 10.1111/risa.13229

Owens, M. J., Lang, M., Barnard, L., Riley, P., Ben-Nun, M., Scott, C. J., ... Gonzi, S. (2020). A computationally efficient, time-dependent model of the solar wind for use as a surrogate to three-dimensional numerical magnetohydrodynamic simulations. *Solar Physics*, *295*. Retrieved from http://dx.doi.org/10.1007/s11207-020-01605-3 doi: 10.1007/s11207-020-01605-3

Owens, M. J., Lang, M., Riley, P., Lockwood, M., & Lawless, A. S. (2020). Quantifying the latitudinal representivity of in situ solar wind observations. *Journal of Space Weather and Space Climate*, *10*. doi: 10.1051/swsc/2020009

Owens, M. J., Lockwood, M., & Barnard, L. A. (2020). The value of cme arrival-time forecasts for space weather mitigation. *Space Weather*. Retrieved from https://onlinelibrary.wiley.com/doi/abs/10.1029/2020SW002507 doi: 10.1029/2020SW002507

Owens, M. J., Merkin, V. G., & Riley, P. (2006). A kinematically distorted flux rope model for magnetic clouds. *Journal of Geophysical Research: Space Physics*, *111*, 1-8. doi: 10.1029/2005JA011460

Owens, M. J., & Riley, P. (2017). Probabilistic solar wind forecasting using large ensembles of near-sun conditions with a simple one-dimensional "upwind" scheme. *Space Weather*, *15*, 1461-1474. doi: 10.1002/2017SW001679

Pant, V., Willems, S., Rodriguez, L., Mierla, M., Banerjee, D., & Davies, J. A. (2016). Automated detection of coronal mass ejections in stereo heliospheric imager data. *The Astrophysical Journal*, *833*, 80. Retrieved from http://dx.doi.org/10.3847/1538-4357/833/1/80 doi: 10.3847/1538-4357/833/1/80

Pizzo, V., Millward, G., Parsons, A., Biesecker, D., Hill, S., & Odstrcil, D. (2011). Wang-sheeley-arge-enlil cone model transitions to operations. *Space Weather*, *9*, 2. doi: 10.1029/2011SW000669

Riley, P., & Gosling, J. T. (1997). By a fast , high-pressure coronal mass ejection. , *102*, –.

Riley, P., & Lionello, R. (2011). Mapping solar wind streams from the sun to 1 au: A comparison of techniques. *Solar Physics*, *270*, 575-592. doi: 10.1007/s11207-011-9766-x

Riley, P., Mays, M. L., Andries, J., Amerstorfer, T., Biesecker, D., Delouille, V.,

… Zhao, X. (2018). Forecasting the arrival time of coronal mass ejections: Analysis of the ccmc cme scoreboard. *Space Weather*, *16*, 1245-1260. doi: 10.1029/2018SW001962

Scott, C. J., Owens, M. J., de Koning, C. A., Barnard, L. A., Jones, S. R., & Wilkinson, J. (2019). Using ghost fronts within stereo heliospheric imager data to infer the evolution in longitudinal structure of a coronal mass ejection. *Space Weather*, *17*, 539-552. doi: 10.1029/2018SW002093

Subramanian, P., & Vourlidas, A. (2007). Energetics of solar coronal mass ejections. *Astronomy and Astrophysics*, *467*, 685-693. doi: 10.1051/0004-6361:20066770

Thomas, S. R., Fazakerley, A., Wicks, R. T., & Green, L. (2018). Evaluating the skill of forecasts of the near-earth solar wind using a space weather monitor at l5. *Space Weather*, *16*, 814-828. doi: 10.1029/2018SW001821

Vourlidas, A. (2015). Mission to the sun-earth l5 lagrangian point: An optimal platform for space weather research. *Space Weather*, *13*, 197-201. doi: 10.1002/2015SW001173

Vršnak, B., Temmer, M., Žic, T., Taktakishvili, A., Dumbović, M., Möstl, C., … Odstrčil, D. (2014). Heliospheric propagation of coronal mass ejections: Comparison of numerical wsa-enlil+cone model and analytical drag-based model. *Astrophysical Journal, Supplement Series*, *213*. doi: 10.1088/0067-0049/213/2/21

Zhang, M., Feng, X. S., & Yang, L. P. (2019). Three-dimensional mhd simulation of the 2008 december 12 coronal mass ejection: From the sun to interplanetary space. *Journal of Space Weather and Space Climate*, *9*, 1-17. doi: 10.1051/swsc/2019034